Journal of Biomedical Optics

BiomedicalOptics.SPIEDigitalLibrary.org

Accurate viscosity measurements of flowing aqueous glucose solutions with suspended scatterers using a dynamic light scattering approach with optical coherence tomography

Andrew Weatherbee
Ivan Popov
Alex Vitkin

SPIE.

Andrew Weatherbee, Ivan Popov, Alex Vitkin, "Accurate viscosity measurements of flowing aqueous glucose solutions with suspended scatterers using a dynamic light scattering approach with optical coherence tomography," *J. Biomed. Opt.* **22**(8), 087003 (2017), doi: 10.1117/1.JBO.22.8.087003.

Accurate viscosity measurements of flowing aqueous glucose solutions with suspended scatterers using a dynamic light scattering approach with optical coherence tomography

Andrew Weatherbee,[a] Ivan Popov,[a] and Alex Vitkin[a,b,c,*]
[a]University of Toronto, Department of Medical Biophysics, Toronto, Ontario, Canada
[b]University of Toronto, Department of Radiation Oncology, Toronto, Ontario, Canada
[c]University Health Network, Ontario Cancer Institute, Division of Biophysics and Bioimaging, Toronto, Ontario, Canada

Abstract. The viscosity of turbid colloidal glucose solutions has been accurately determined from spectral domain optical coherence tomography (OCT) M-mode measurements and our recently developed OCT dynamic light scattering model. Results for various glucose concentrations, flow speeds, and flow angles are reported. The relative "combined standard uncertainty" $u_c(\eta)$ on the viscosity measurements was $\pm 1\%$ for the no-flow case and $\pm 5\%$ for the flow cases, a significant improvement in measurement robustness over previously published reports. The available literature data for the viscosity of pure water and our measurements differ by 1% (stagnant case) and 1.5% (flow cases), demonstrating good accuracy; similar agreement is seen across the measured glucose concentration range when compared to interpolated literature values. The developed technique may contribute toward eventual noninvasive glucose measurements in medicine. [DOI: 10.1117/1.JBO.22.8.087003]

Keywords: optical coherence tomography; dynamic light scattering; Brownian motion; speckle; viscosity; glucose.

Paper 170130RR received Feb. 24, 2017; accepted for publication Jul. 18, 2017; published online Aug. 31, 2017.

1 Introduction

Recently, there has been significant interest in studying the properties of coherent radiation scattered from Brownian particles under optical coherence tomography (OCT) conditions. This interest has been motivated by a wide range of emerging biomedical applications, including capillary velocimetry,[1,2] biofilm growth measurement,[3] OCT angiography and lymphangiography,[4–6] subcellular metabolic contrast imaging,[7] intracellular dynamics measurements,[8] and noninvasive blood glucose monitoring.[9] The coherent radiation scattered from Brownian particles contains information about the suspending fluid, such as viscosity and flow parameters, and about the scattering particles themselves, such as their size and shape. For example, when the suspending fluid is stagnant, well-established dynamic light scattering (DLS) theory allows the fluid viscosity to be determined via measurement of the Lorentzian power spectrum of the scattered radiation;[10] increasing the viscosity of the fluid decreases the random Doppler shifts introduced by the Brownian particles and narrows the measured power spectrum.

However, if the fluid is flowing, one needs to take into account the additional spectral broadening that results from the flow-caused speckle fluctuations recorded by the detector. Modeling the OCT voxel with a two-dimensional Gaussian illumination intensity profile in the transverse plane and a Gaussian response profile along the axial direction (coherence length of the OCT light source), it has been shown that this additional spectral broadening due to flow produces a Gaussian shape in the measured power spectrum.[11,12] The combination of the Brownian motion and flow processes can thus be represented by the frequency space convolution of the corresponding Lorentzian and Gaussian line shapes, yielding the so-called Voigt spectrum.[12] Measurement of this Voigt spectrum under OCT conditions allows for measurements of diffusivity and flow velocity.[13–17] The ability to make accurate measurements of fluid viscosity under both stagnant and flowing conditions is important for a number of biomedical applications, including noninvasive blood glucose monitoring. In addition to glucometry, increased blood viscosity is also important in cardiology—it has been linked to many major cardiovascular risk factors, including metabolic syndrome, type-II diabetes, elevated low-density lipoprotein and low high-density lipoprotein cholesterol levels, high blood pressure, obesity, and smoking.[18,19] Given the tremendous importance and significant challenges inherent in the unmet clinical need, noninvasive glucometry is an active area of OCT research.[20–23] Currently, two OCT-based approaches are explored for noninvasive glucometry in blood, based on signal attenuation[24–26] and correlation function analyses.[9,27,28] However, accuracy, robustness, and sensitivity/specificity are currently insufficient for clinical implementations, for example, in diabetic patients use. Specifically, attenuation techniques are complicated due to the attenuation as a function of glucose concentration having considerable fluctuations;[29] therefore, this approach does not appear promising for use in clinical practice. In this paper, we thus pay particular attention to quantifying the measurement error and "combined standard uncertainty"[30] (u_c) of our OCT fluid viscosity determination. The employed uncertainty analysis is based on the widely accepted guide to the expression of uncertainty in measurement (GUM) standards.[30]

*Address all correspondence to: Alex Vitkin, E-mail: vitkin@uhnres.utoronto.ca

1083-3668/2017/$25.00 © 2017 SPIE

Much of the existing research on viscosity measurements of aqueous glucose solutions at low (mM range) concentrations comes from the food industry.[31,32] However, these studies typically do not report the errors or uncertainty of their measurements; further, reported viscosity values are often in conflict. For example, one food industry publication[33] (which in fact does report measurement uncertainty) provides an equation for viscosity as a function of temperature and glucose concentration, yet the equation's predictions do not agree with viscosity data in a standard reference handbook.[34]

The typical method to determine fluid viscosity is by use of a viscometer, whereby the drag resistance during relative motion of a stationary object and flowing fluid allow the viscosity of the latter to be determined. For example, one can measure the time taken for a fluid volume to pass through a capillary of a given diameter and then analyze the data via well-known fluid mechanics formulas. However, viscometer measurements are essentially impossible to perform *in situ* or *in vivo*. Conversely, DLS OCT methodology measures coherent radiation scattered by an intact sample and holds promise for noninvasive measurement of fluid viscosity and potentially even *in vivo* glucose concentration measurements.[22]

The present research thus has two objectives. First, we demonstrate DLS M-mode OCT measurements of backscattered radiation spectra to determine the viscosity of a suspending fluid with good accuracy and low uncertainty. Specifically, we measure the viscosity of aqueous glucose solutions over the concentration range of 0 to 1600 mM glucose with a relative combined standard uncertainty [relative $u_c(\eta)$] of $\pm 1\%$ (1 part in 100) under stagnant (no-flow) conditions and $\pm 5\%$ (1 part in 20) under flowing conditions, where relative $u_c(\eta)$ is defined as $[u_c(\eta)/\text{mean}(\eta)] \times 100\%$. These are robust results, the uncertainty being considerably lower than previous reports.[13] Second, we experimentally validate a mathematical model, which was recently developed to describe the statistical properties of radiation scattered from flowing Brownian particles, not only in the focal plane of an OCT optical system but also outside of it.[12,35] It is stressed in recent publications[36,37] that there is a lack of experimentally validated quantitative models for OCT measurements of flowing Brownian particles, and this paper helps to address this need. Our theoretical formalism does indeed describe the data well, and the resultant fitting parameters (which enable determination of fluid viscosity) agree with literature and also offer a significant improvement in uncertainty.

2 Experimental Setup

A research fiber-based spectral domain OCT (SD-OCT) system, operating in M-mode, was used for this study (Fig. 1). Its detailed description is given in Ref. 38; the main points are briefly highlighted here. The system is powered by a superluminescent diode unit (D-1300 Superlum Ltd.) with emission bandwidth of 121.5 nm full width at half maximum, centered at 1313.1 ± 0.07 nm[39] and 12 mW output power. The detection module is comprised of a high-resolution spectrometer (P&P Optica) interfaced with a 1024 pixel, linear array near-infrared CCD camera (SU1024LDH-1.7 μm, UTC Aerospace Systems) with a readout rate selected to be 1123 or 2237 Hz for all experiments described below.

In the sample arm, the radiation is emitted from the single-mode fiber and shaped by an optical system, including an objective lens with a 20 mm focal length, which produces a Gaussian beam with a radius w_0 of 11.5 ± 0.3 μm at the waist in air, so

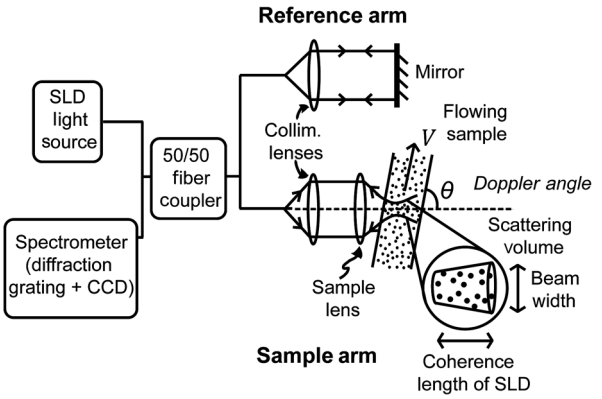

Fig. 1 OCT setup.

that the transverse resolution is 23 μm. The beam profile was characterized using a scanning slit optical beam profiler (Thorlabs Inc.). The axial OCT resolution defined by the source coherence length l_c was measured using a front-surface mirror, yielding $(l_c)_0 = 13.0 \pm 0.5$ μm full width at $1/e$ OCT signal level in air. The Rayleigh range of the beam in water was $z_F = \frac{\pi n w_0^2}{\lambda_0} = 415$ μm, where $n = 1.320 \pm 0.001$ is the water refractive index at $\lambda_0 = 1313.1$ nm.[40,41] To avoid the impact of the point spread function tail truncation along the sample arm axis by the walls of the glass capillary, data collection was restricted to be within ~40 μm of the capillary center.

Distilled water was mixed with powdered D-(+)-glucose (Dextrose) (Sigma-Aldrich Inc.) to prepare eight phantoms with the following concentrations: 0, 25, 50, 100, 200, 400, 800, and 1600 mM glucose. Polystyrene microspheres (Bangs Laboratories Inc.) of radius $R = 107.6 \pm 0.8$ nm[42] were then suspended in each phantom at a concentration of 0.5% by volume, this scatterer concentration was chosen to avoid complications due to multiple scattering effects. The scattering coefficients for the phantoms, calculated via Mie theory, were from 0.24 cm^{-1} (glucose free) down to 0.18 cm^{-1} (1600 mM); this variation in μ_s for a constant concentration of scattering microparticles is due to the glucose's refractive index matching effect.[34] All phantoms appeared opaque and milky-white to the naked eye as they contained ~5000 spheres per voxel, and can be considered turbid colloidal suspensions.[43] A microbore glass capillary with an inner diameter of 165 ± 1 μm (Accu-Glass Inc.) was used to house the glucose + microsphere mixtures in water. The flow was driven by a syringe pump actuated by a stepper motor operating in 17 nm steps at ~1 ms per step (New Era Pump Systems Inc.), effectively enabling continuous flow. In the flow experiments, the velocity at the capillary center was calculated to be 1.94 ± 0.01 mm/s using the volume flow rate from the syringe pump and the Poiseuille parabolic velocity profile equation for laminar flow through a cylinder. This flow speed was chosen so that the contributions to spectrum broadening were similar from both the Brownian motion (random Doppler shifts) and the flow (translational speckle motion).

The first data set was recorded from the scattering phantoms under stagnant (no-flow) conditions with an A-scan sampling rate of 1123 Hz and total sampling time of ~7 minutes per phantom. The perpendicular-flow data set was recorded in the same way. The angled-flow data set (81° between the optical axis and the flow direction) used a sampling rate of 2237 Hz for a total of

~7 minutes per phantom. For each A-scan, 1024 spectrum amplitude values were obtained on an equally spaced wavevector scale; the inverse Fourier transform produced 512 complex values, as a function of depth into the sample. Repeated A-scans meant that the complex OCT signal (real and imaginary parts of the field scattered from the voxel) was sampled as a function of time, and the power spectrum (frequency-space, f) of the scattered field was found by taking the square modulus of the Fourier transform of the real part (time-space, t) of the complex OCT signal. It was demonstrated in Ref. 13 that even with a flowing sample, the temporal correlation function (and consequently the power spectrum) does not depend on the distance between the scattering volume and the beam waist; thus, there was no need to accurately position the scattering volume to a specific depth within the capillary (such as placing the beam waist at the center of the capillary or any other position of interest).

3 Spectral Properties of the Radiation Scattered from Stagnant and Flowing Brownian Particles

3.1 *No-Flow Conditions*

Here, we briefly summarize some background theoretical results from Refs. 10, 12, and 35 needed to calculate the viscosity of a *stagnant* fluid from coherent light scattering measurements. This is a well-established problem in DLS theory;[10] the more viscous the fluid, the slower are the speeds of the Brownian particles suspended in it, resulting in smaller Doppler shifts in the scattered radiation and a narrower power spectrum. Under stagnant conditions, DLS theory states that the power spectrum can be described by a Lorentzian function[10]

$$L(f) = \frac{1}{\left(\frac{1}{2\pi\tau_b}\right)^2 + f^2}, \tag{1}$$

where $\tau_b = \frac{1}{4k^2D}$ is the decay time constant (under heterodyne conditions) due to Brownian motion, $k = \frac{2\pi}{\lambda}$, λ is the light wavelength in the suspending fluid, D is the spherical particle diffusivity given by the Einstein–Stokes equation $D = \frac{k_B T}{6\pi\eta R}$, k_B is the Boltzmann's constant, T is the absolute temperature, η is the liquid viscosity, and R is the particle radius. The half width at half maximum ($HWHM_b$) of the Lorentzian in Eq. (1) is given by

$$HWHM_b = \frac{1}{2\pi\tau_b} = \frac{2k^2D}{\pi} = \frac{k^2 k_B T}{3\pi^2\eta R}. \tag{2}$$

Thus, given the radius of the spherical Brownian scatterers and knowing the experimental temperature, the viscosity of the suspending fluid can be determined by fitting a Lorentzian to the experimentally measured power spectrum, determining its $HWHM$ and solving Eq. (2).

3.2 *Flowing Conditions*

In the case of Brownian particles suspended in a *flowing* fluid, the mathematical model for the power spectrum must take into account two sources of spectral broadening: the first is due to the random Doppler shifts caused by the Brownian motion as discussed above and the second is due to the dynamic speckle pattern on the detector that results from the flow.[44] Recently, both of these effects have been taken into account under OCT conditions.[12,11,35] In particular, Eq. (18) from Ref. 12 provides a mathematical expression that models the power spectrum of the scattered optical field using a Voigt function, which is the convolution in frequency space of a Lorentzian Eq. (1) (Brownian Doppler broadening) with a Gaussian[12] that may be Doppler shifted $G(f - f_D) = \exp\{-[\pi\tau_t(f - f_D)^2]\}$ (translational speckle fluctuation broadening), where f_D is the Doppler shift due to flow, $f_D = \frac{2v_z}{\lambda}$, $\lambda = \frac{\lambda_0}{n}$, and v_z is the flow velocity component in the axial direction ($v_z = 0$ for the special case of perpendicular flow). The Voigt function, $W(f - f_D)$, can be expressed analytically in terms of the complex error function erf[12]

$$W(f - f_D) = \mathrm{Re}\left(\sqrt{\frac{\pi}{4\frac{\tau_b}{\tau_t}}}\exp\left\{\left[\frac{1 - i2\pi\tau_b(f - f_D)}{2\frac{\tau_b}{\tau_t}}\right]^2\right\} \times \left\{1 - \mathrm{erf}\left[\frac{1 - i2\pi\tau_b(f - f_D)}{2\frac{\tau_b}{\tau_t}}\right]\right\}\right), \tag{3}$$

where $i = \sqrt{-1}$ and τ_t is the decay time constant due to translational flow motion, given by[12,35]

$$\tau_t = \left[\frac{v_x^2 + v_y^2}{w_0^2} + \frac{1}{2}\left(\frac{v_z}{l_c/2}\right)^2\right]^{-1/2} = \left(v^2\left\{\left[\frac{\sin(\theta)}{w_0}\right]^2 + \frac{1}{2}\left[\frac{\cos(\theta)}{l_c/2}\right]^2\right\}\right)^{-1/2}, \tag{4}$$

where v_x and v_y are the transverse components of the flow velocity, θ is the Doppler angle (angle between OCT interrogation/detection optical axis and flow direction), l_c is the coherence length of the light source, and w_0 is the Gaussian beam radius at the waist. The values of these parameters are known/calculated/measured in the analysis that follows.

The challenges in fitting the Voigt function [Eq. (3)] to data using a least squares approach are well-known in the literature.[45–48] One problem is that Eq. (3) contains a product of an exponential and complementary error function of the same argument, $\frac{1-i2\pi\tau_b(f-f_D)}{2\frac{\tau_b}{\tau_t}}$; as the argument grows (with increasing frequency in the fitting region), the exponential rapidly increases, while the complementary error function rapidly decreases, causing stability problems in the fitting procedure for large f [$f > 500$ Hz was problematic for fitting Eq. (3) in our data]. To fit the full spectra, we used the MATLAB® algorithm from Ref. 47, which is accurate to within 10^{-13}.

This summarizes the main theoretical predictions from Refs. 10, 12, and 35 needed to calculate the viscosity of a fluid from coherent light scattering measurements. In Sec. 4 below, the viscosities of fluid samples are determined by fitting Eq. (1) (no-flow case) and Eq. (3) (flow cases) to our experimental spectral data and then using Eq. (2) to calculate the viscosity of the fluid samples. We note that the τ_b in Eq. (3) is identical to the τ_b in Eq. (1); this is because Eq. (3) was derived via a convolution in frequency space of Eq. (1) and a Gaussian function, as described above.

4 Results and Discussion

4.1 *No-Flow Case*

To determine the sample viscosity for the no-flow case, we fit Eq. (1) to the experimentally obtained power spectra with τ_b as

the only fitting parameter and then use Eq. (2) to compute the viscosity. Figure 2(a) shows the experimentally obtained power spectra for a single depth in the sample, with Eq. (1) fitted (solid lines) for each glucose concentration. As seen, the fit is good throughout the studied concentration range. The derived results from the experimental fits of Fig. 2, as well as from additional glucose concentrations, are shown in Table 1 (top rows). Our determined viscosity value for pure water is (0.904 ± 0.008) mPa · s, which is within ~1% of the accepted literature value at 23.8°C of $((0.914 \pm 0.0005)$ mPa · s[49] (see Table 1), indicating high accuracy for our methodology in turbid water suspensions under no-flow conditions. Assessing the accuracy of the glucose results is more challenging, owing to the incomplete (and often conflicting, see discussion in Sec. 1) set of literature values for comparison. We thus used an interpolation method (explained in more detail below) to generate "literature values" at 23.8°C from the existing 20°C and 30°C literature data (Refs. 34 and 50, respectively). The resulting values are shown in the bottom row of Table 1. Comparing the top and bottom row entries across the measured glucose concentration range, we note an accuracy of $\sim \pm 1\%$ in the no-flow colloidal glucose suspensions, except for the 1600 mM value which differs by ~2.5%.

In the no-flow case, the spectrum broadening is caused solely by the axial component of the random Doppler shifts produced by the jittering Brownian particles. Therefore, we would expect the $HWHM_b$ of the measured Lorentzian power spectra to be independent of depth into the sample. Indeed, aside from some statistical variation, this independence of depth is shown in Fig. 2(b), which plots the $HWHM_b$ values of the fitted Lorentzian as a function of depth across the capillary, with respect to the center of the capillary. Since the spectral width does not depend on the z-coordinate, the measured viscosity [calculated via Eq. (2)] also exhibits no depth dependence, as expected (mean values across depths are presented in Table 1).

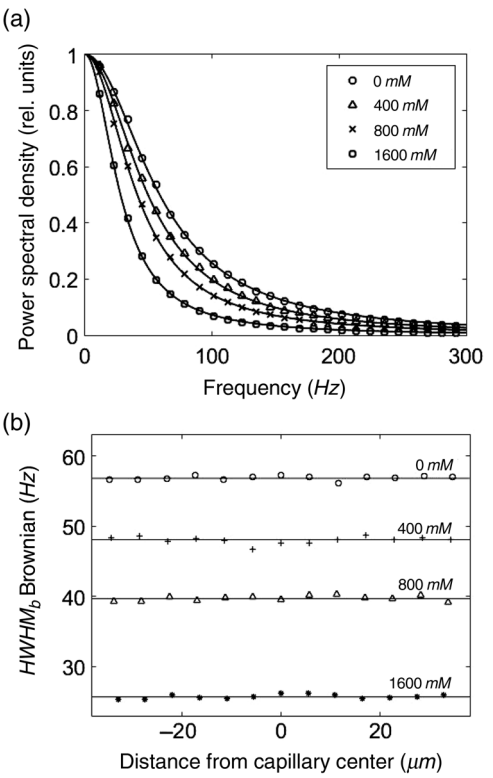

Fig. 2 (a) Power spectra of backscattered radiation from Brownian particles (polystyrene microspheres) suspended in stagnant aqueous glucose solutions in the 0 to 1600 mM range. Symbols are experimentally obtained power spectrum values and lines are theoretical fits of Eq. (1) with τ_b as the fitting parameter. (b) $HWHM_b$ of the power spectra in (a), as a function of depth in the capillary. Symbols are the $HWHM_b$ values from the theoretical fits of Eq. (1) and lines are the average fitted values for each concentration.

4.2 *Perpendicular Geometry Flow Case*

For these experiments, the direction of flow was set perpendicular to the OCT sample arm beam axis, by minimizing the Doppler shift in the power spectrum (i.e., having the peak centered at $f_D \to 0$). The viscosity of each sample was determined by fitting an algorithm approximation[45,47] of Eq. (3) to the measured power spectra and then using Eq. (2) to compute the viscosity for each depth. Figure 3(a) shows the experimentally obtained power spectra from the OCT voxel located at the center of the glass capillary, for different glucose concentrations. The lines in Fig. 3(a) are the fits of the algorithm approximation of Eq. (3) to the spectra, with both τ_t and τ_b as fitting parameters. As seen, Eq. (3) describes the data well across all measured glucose concentrations. The middle rows in Table 1 show the resulting numbers derived from these fits, averaged across all depths. Comparing to the top-row (no-flow) results, we note the consistency of our methodology in determining viscosity values under these two different experimental conditions. Comparing to the literature values bottom row, we note the technique's accuracy for glucose viscosity determination under the perpendicular-flow conditions.

Figure 3(b) plots the Brownian motion contribution ($HWHM_b$) to the width of the fitted Voigt as a function of depth in the capillary; as expected, viscosity was independent of depth. Further, calculation of the flow speed v via Eq. (4) using the fitted τ_t values as a function of depth showed good agreement with the theoretically expected parabolic flow profile (with <5% RMS deviation from the expected flow profile over all depths, for each glucose concentration—data not shown). The good fits in the presence of flow, the depth independence of the results, and the close agreement with literature values all validate our recently proposed mathematical OCT DLS model.[12,35]

4.3 *Doppler Angle Flow Case*

Having examined the special cases of no-flow and perpendicular-flow situations, we now move on to the most general case, with flow at an arbitrary (non-perpendicular) angle. Here, we must take into account the Doppler shifted peak centered at f_D due to the axial flow component. In OCT, we measure both the amplitude and phase of the scattered electric field. However, in our data analysis, we are using only the real part of the electric field sampled in time (purely, real function of time), the Fourier transform of which is Hermitian, resulting in a power spectrum that is symmetric about the $f = 0$ baseband. Therefore, when performing the fitting, we need to include the peak shifted to the negative frequencies, and the fitting function in Eq. (3) becomes

$$W_D(f) = W(f - f_D) + W(f + f_D), \tag{5}$$

where $W(f - f_D)$ is defined in Eq. (3), and $W(f + f_D)$ is a "mirror" image peak that appears in the negative frequencies. This means that in the positive frequencies (ones with physical meaning) there is the dominant contribution from the Voigt peak

Table 1 Brownian contributions to measured spectral widths $HWHM_b$ and corresponding viscosity and diffusivity values [via Eq. (2)] in stagnant and flowing suspensions of microspheres in water with varying amounts of dissolved glucose. All numbers following the ± symbols are the numerical values of the combined standard uncertainty.[30]

Glucose concentration	mM	0	25	50	100	200	400	800	1600
n-refractive index		1.320	1.321	1.321	1.322	1.325	1.330	1.339	1.355
No-flow case									
$HWHM_b$ of fitted Lorentzian ± $u(HWHM_b)$ [a] (averaged in depth)	Hz	56.83 ± 0.03	56.21 ± 0.03	55.72 ± 0.03	54.49 ± 0.03	52.30 ± 0.03	47.95 ± 0.03	39.70 ± 0.02	25.67 ± 0.01
Diffusivity ± $u_c(D)$	$\frac{\mu m^2}{s}$	2.238 ± 0.005	2.213 ± 0.005	2.194 ± 0.005	2.145 ± 0.005	2.059 ± 0.005	1.888 ± 0.004	1.563 ± 0.004	1.011 ± 0.002
Viscosity ± $u_c(\eta)$	mPa · s	0.904 ± 0.008	0.914 ± 0.008	0.922 ± 0.008	0.942 ± 0.008	0.982 ± 0.008	1.071 ± 0.009	1.294 ± 0.011	2.001 ± 0.017
Perpendicular geometry flow case									
Two-parameter fit: τ_b and τ_t were fit simultaneously via an algorithm approximation[45,47] of Eq. (3)									
$HWHM_b$ of fitted Voigt ± $u(HWHM_b)$ [b] (averaged in depth)	Hz	56.6 ± 0.4	56.1 ± 0.3	56.1 ± 0.5	54.6 ± 0.2	53.1 ± 0.9	48.5 ± 0.6	40.7 ± 1.1	26.6 ± 1.0
Diffusivity ± $u_c(D)$	$\frac{\mu m^2}{s}$	2.23 ± 0.01	2.21 ± 0.01	2.21 ± 0.02	2.15 ± 0.01	2.09 ± 0.04	1.91 ± 0.03	1.60 ± 0.05	1.05 ± 0.04
Viscosity ± $u_c(\eta)$	mPa · s	0.91 ± 0.01	0.92 ± 0.01	0.92 ± 0.01	0.94 ± 0.01	0.97 ± 0.02	1.06 ± 0.02	1.26 ± 0.04	1.93 ± 0.07
Doppler angle flow case ($\theta = 81°$)									
Three-parameter fit: τ_b, f_D, and τ_t were fit simultaneously via an algorithm approximation[45,47] of Eq. (5)									
$HWHM_b$ of fitted Voigt ± $u(HWHM_b)$ [b] (center of capillary)	Hz	57.1 ± 0.9	58.7 ± 3.3	54.6 ± 1.8	56.9 ± 3.2	56.6 ± 5.1	48.2 ± 0.8	39.4 ± 1.1	28.8 ± 3.8
Diffusivity ± $u_c(D)$	$\frac{\mu m^2}{s}$	2.25 ± 0.04	2.31 ± 0.13	2.15 ± 0.07	2.24 ± 0.13	2.23 ± 0.20	1.90 ± 0.03	1.55 ± 0.04	1.13 ± 0.15
Viscosity ± $u_c(\eta)$	mPa · s	0.90 ± 0.02	0.87 ± 0.05	0.94 ± 0.03	0.90 ± 0.05	0.91 ± 0.08	1.06 ± 0.02	1.30 ± 0.04	1.78 ± 0.24
Existing literature values									
Literature viscosity values at 23.8°C	mPa · s	0.914[c]	0.91[d]	0.92[d]	0.94[d]	0.98[d]	1.07[d]	1.29[d]	1.95[d]

[a] $u(HWHM_b) \equiv fitting\ uncertainty$.

[b] $u(HWHM_b) \equiv \sqrt{(fitting\ uncertainty)^2 + \left((\eta_{flow} - \eta_{no\text{-}flow})\right)^2}$.

[c] Reference 49.

[d] Literature values interpolated from 20°C (Ref. 34) and 30°C data (Ref. 50)

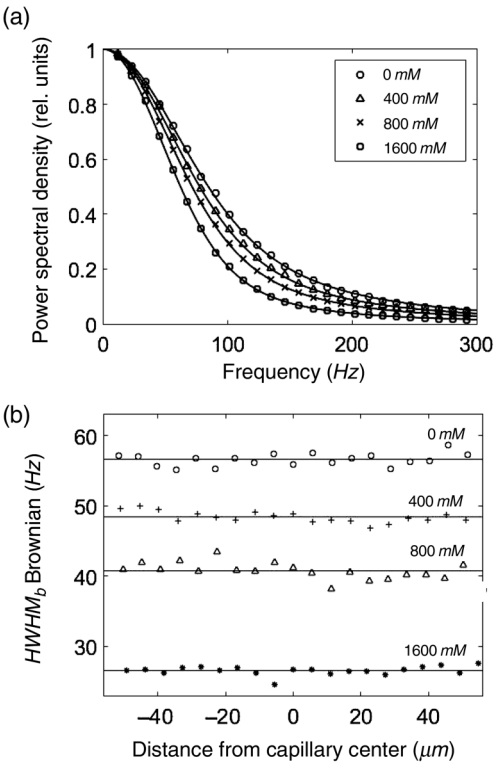

Fig. 3 (a) Analogous to Fig. 2(a) but now with flow perpendicular to the OCT sample arm beam. Symbols are experimentally obtained power spectrum values and lines are the fits of the algorithm approximation of Eq. (3) to the spectra with both τ_t and τ_b as fitting parameters. (b) Brownian motion contribution ($HWHM_b$) to power spectra in (a), as a function of depth across the capillary. Symbols are the $HWHM_b$ calculated via Eq. (2), using τ_b values from the fits of Eq. (3) and lines are the average $HWHM_b$ for each glucose concentration.

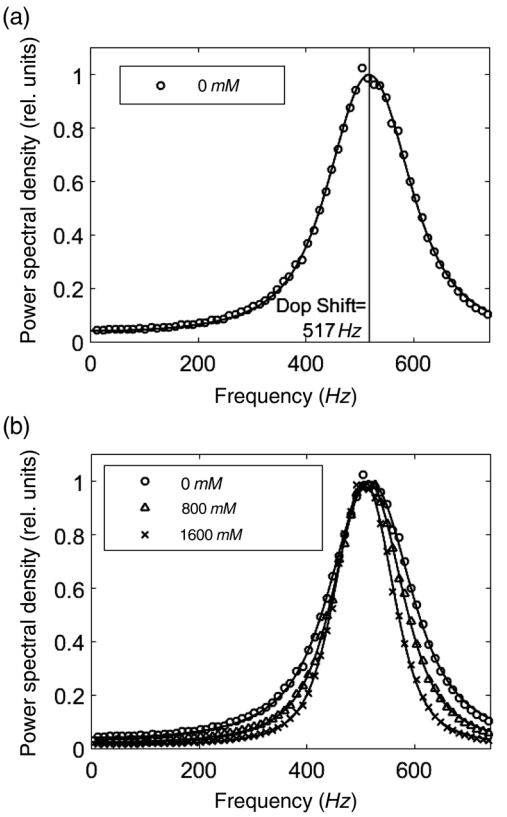

Fig. 4 Power spectra of backscattered radiation from flowing Brownian particles (polystyrene microspheres) in the aqueous glucose solutions, with a Doppler angle $\theta = 81°$ in air. Data were collected from the center of capillary voxel, where the flow speed was $v = 1.94$ mm/s and the velocity gradients were minimal. Symbols are experimentally obtained power spectrum data, and the fits of the algorithm approximation to Eq. (5) are shown as solid lines (where f_D, τ_t, and τ_b are the fitting parameters). (a) 0 mM glucose, (b) 100, 800, and 1600 mM glucose.

that was shifted to the positive frequencies but also a contribution from the tail of the "mirror" Voigt peak in the negative frequency space. This "mirror component" effect can be significant, especially when the Doppler shift is comparable to the width of the peak (results not shown for brevity but most pronounced for slow flows, voxel location close to capillary wall, or θ close to 90°).

We now determine the viscosity of each phantom, starting by fitting Eq. (5) (via the algorithm approximation)[45,47] to the spectrum data. The Doppler angle θ chosen for the experiments was 81° in air. Figure 4 plots the experimentally obtained power spectrum from the voxel at the center of the glass capillary with the 0 mM data in Fig. 4(a) and the 100, 800, and 1600 mM data in Fig. 4(b). The lines in Fig. 4 show the fits of Eq. (5) with f_D, τ_t, and τ_b as the fitting parameters. As seen, the fit is good for all glucose concentrations. The lower rows in Table 1 show the resulting derived values. Comparing to the top-row (no-flow) results, we again note the consistency of our methodology in determining viscosity values under these different experimental conditions. Comparing to the literature values in the bottom row, we note the technique's accuracy for glucose viscosity determination under the Doppler angle-flow conditions. Specifically, for the case of pure water, the well-established literature value of 0.914 mPa · s differs by ~1.5% from our flow measurements. This experimental consistency and good accuracy further validate the mathematical OCT DLS model originally developed in Refs. 12 and 35.

Assuming a parabolic flow profile, we calculated $v = 1.94$ mm/s at the center of the capillary, and the expected Doppler peak position for 0 mM glucose from the Doppler shift formula is $f_D = \frac{2v_z n}{\lambda_0} = 518$ Hz. This is in very close agreement with the best-fit peak position as shown in Fig. 4(a). Further, note that the positions of the Doppler peaks in Fig. 4(b) are not identical for the various glucose concentrations, for two reasons. First, the position of the Doppler peak depends on the glucose concentration through the refractive index, both directly in the formula $f_D = \frac{2v_z n}{\lambda_0}$, as well as indirectly through v_z (which depends on the Doppler angle in air and the refractive index of the suspending fluid). Second, the flow speeds in each of the experiments were likely not exactly the same: slight average flow speed variations do not significantly impact the measured width of the peak, and thus do not impact the measured viscosity values, yet the position of the peak in the frequency domain is very sensitive to these slight flow variations. Overall though, increasing glucose concentration narrows the spectral width of the peak, as expected from increasing viscosity which dampens the Brownian motion of the scatterers; the fact that we can measure and quantify this effect even under angled-flow conditions is encouraging.

We also point out that for the angled flow case, even slight velocity gradients within the OCT measurement voxel will cause

artifacts.[11] In fact, the only depth in the capillary where it was possible to accurately measure the viscosity was at its center position, where the velocity gradient of the parabolic flow profile was close to zero. For all other depths, the velocity gradient is enough to cause additional spectral broadening and thus yield inaccurate results. Within 40 μm from the center of the capillary, the velocity gradient causes a change in the Voigt spectral width (departure from theory) of up to 7%.

4.4 *Measurement Uncertainty Analysis*

Here, we briefly explain our uncertainty calculations. We can solve Eq. (2) for viscosity $\eta = \frac{4k_B T n^2}{3\lambda_0^2 R \cdot HWHM_b}$ and diffusivity $D = \frac{\lambda_0^2 \cdot HWHM_b}{8\pi n^2}$; aside from the constant k_B, each variable in the RHS of these equations has an associated "standard uncertainty, u" (the standard deviation of the assumed probability distribution of the variable, either measured directly, provided by the manufacturer, or estimated). GUM details how to mathematically combine these individual standard uncertainties to produce the combined standard uncertainty, u_c, on viscosity, $u_c(\eta)$, and on diffusivity, $u_c(D)$. By applying the GUM procedure, we assume that these individual components of uncertainty are statistically independent.

Table 1 presents a results summary. It lists the $HWHM_b$ values and corresponding diffusivity and viscosity values for all three experimental conditions. For the first $HWHM_b$ row (no-flow case), the numbers following the $\pm$ symbols are the numerical values of the standard uncertainty, $u(HWHM_b)$, calculated directly from the confidence interval (from the MATLAB® fitting procedure) on the fitted parameter τ_b; thus, $u(HWHM_b)$ is a measure of the quality of the fit of the Lorentzian to the data. The MATLAB® fitting procedure assumes that the fitted parameter τ_b is a Gaussian random variable.

For the second and third $HWHM_b$ rows (flow cases), the numbers following the $\pm$ symbols are the numerical values of the standard uncertainty $u(HWHM_b)$, which we assume has two contributions: $u(HWHM_b)_{flow} \equiv \sqrt{(random\ component)^2 + (biased\ component)^2}$. The first is the (random) fitting uncertainty on $HWHM_b$ calculated directly from the confidence interval (from the MATLAB® fitting procedure) on the fitted parameter τ_b. The second is a non-random component (bias component), which we estimate as the difference between the measured $HWHM_b$ values and the no-flow $HWHM_b$ values: $|\eta_{\text{perp-flow}} - \eta_{\text{no-flow}}|$ for the perpendicular-flow values and $|\eta_{\text{angled-flow}} - \eta_{\text{no-flow}}|$ for the angled flow values.

For the no-flow and perpendicular-flow cases, the listed $HWHM_b$ values are averages taken over depths within ~40 μm from the capillary center. For the $\theta = 81°$ experiment, only the data from the center of capillary location are listed. To calculate the combined standard uncertainties for diffusivity $u_c(D)$ and viscosity $u_c(\eta)$, for all three experimental conditions, the following values and their associated standard uncertainties were used: $T = (23.8 \pm 0.2)$°C, $\lambda_0 = (1313.1 \pm 0.07)$ nm,[39] $n = 1.320 - 1.355 \pm 0.001$,[40,41] and $R = (107.55 \pm 0.75)$ nm,[42] along with the $u(HWHM_b)$ values described above. Although the following uncertainties are not used in our uncertainty calculations, we list them for completeness: $w_0 = (11.5 \pm 0.2)$ μm,[51] $\theta = (81 \pm 1)°$, and $v = 0 - 1.94$ mm/s with a relative standard uncertainty of 1%.[52]

Despite the close agreement in the derived viscosity between the no-flow, perpendicular-flow, and Doppler angle flow cases, the no-flow data have a much smaller $u_c(\eta)$. In fact, the (random) component of uncertainty for the $HWHM_b$ due to the spectral fitting was very similar for all three experiments—the no-flow data fits [Lorentzian, Eq. (1)] and the flow data fits [Voigt, algorithm approximation for Eq. (3)]. The larger uncertainty values under flowing conditions arise from the bias component (discussed above), which is likely caused by some departure of the beam from a Gaussian profile due to spatial noise, and some fluctuations in the flow velocity. In the no-flow case, the main factor limiting the accuracy of viscosity measurements is the uncertainty on the particle radius. All the other components contributing to the combined uncertainty (T, n, λ_0, and $HWHM_b$) are considerably smaller.

As an aside, we note that to produce the averaged spectrum with less fluctuations, it is important to have enough scatterers in the scattering volume, ~100 or more [we used ~5000 per voxel to get high signal to noise (S/N)]. With smaller numbers, the scattering becomes non-Gaussian,[53] and the noise fluctuations in the measured signal (and resulting power spectrum) become considerably higher, which will lead to a larger contribution from the (random) fitting uncertainty.

4.5 *Comparison with Literature*

We begin this section with a brief comparison of our uncertainty values with those published in a previous OCT study,[13] where the diffusivity of spherical Brownian particles in water was measured. First, under no-flow conditions and using a single parameter fit of τ_b, the standard uncertainty on the measurement of diffusivity in Ref. 13 is ~30× higher than the calculated standard uncertainty in this paper (see Table 1). Second, under perpendicular-flow conditions and using a two-parameter fit of τ_b and τ_t, the standard uncertainty on the measurement of diffusivity in Ref. 13 is ~3× higher than the calculated standard uncertainty in this paper.

Next, we compare our measured viscosity values with literature, and thus establish the technique's accuracy. Since there are no reliable data in the literature for the viscosity of aqueous glucose solutions at our experimental temperature of 23.8°C, we used data sources at 20°C (Ref. 34) and at 30°C (Ref. 50), along with the following (slightly modified) empirical equation from Ref. 54 and also used in Ref. 32

$$\eta(x) = \eta_0(1 + cxe^{cx}), \tag{6}$$

where η is the viscosity in mPa · s, η_0 is the viscosity of pure water at the chosen temperature, and x is the molality of the glucose solution. Equation (6) was fit to the literature data for 20°C (top dashed curve in Fig. 5) and for 30°C (bottom dashed-dot curve), with each fit producing a value for the fitted parameter c. The solid middle line in Fig. 5 plots Eq. (6) using the value of c calculated by linearly interpolating (to 23.8°C) the fitted c values from the 20°C and 30°C data, and η_0 set to the viscosity of water at 23.8°C. All reported experimental viscosity results are also plotted as symbols in Fig. 5. These closely follow the solid line prediction and thus graphically demonstrate the good accuracy of the technique. The tight data spread at each glucose concentration also illustrates the good precision of the approach. The inset shows these two findings at the lower glucose concentration range of potential biomedical relevance.

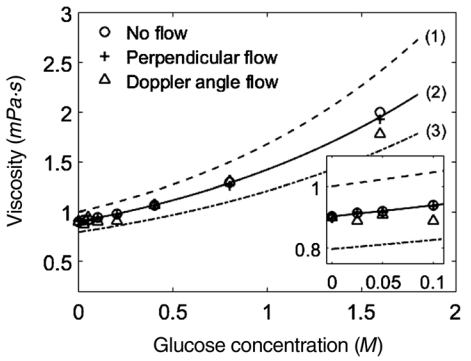

Fig. 5 Graphical summary of all viscosity data and comparison with literature. No-flow (circles), perpendicular-flow (crosses), and Doppler angle flow values (triangles) are the experimentally measured viscosity results summarized in Table 1. Theoretical curves: (1) resulting fit of Eq. (6) to viscosity data from Ref. 34 (top dashed curve, 20°C), (2) resulting fit of Eq. (6) to viscosity data from Ref. 50 (bottom dashed-dot curve, 30°C), (3) Eq. (6) with the parameter value c calculated by linearly interpolating the fitted c values from the 20°C and 30°C fits to 23.8°C and with η_o set to the viscosity of water at 23.8°C (solid curve). The inset shows a zoomed-in view in the lower glucose concentration range of potential biomedical relevance.

We now discuss briefly blood viscosity and follow this with a discussion of the potential of our methodology for *blood* glucometry measurements. The biomedically relevant range of blood viscosity is from 3 to 50 mPa · s.[55] The largest modifier of blood viscosity is blood shear rate, which becomes important in small capillaries under systolic conditions. Models that take into account the impact of shear rate on viscosity are well-developed;[55] this will be considered in our future theoretical model developments. Other important factors affecting blood viscosity are hematocrit and erythrocyte aggregation (rouleaux formation).[18,19] These depend on glucose only slightly and can be measured independently.[56] Further, in diabetic patients, it has been demonstrated that an increase in blood glucose concentration from 5 to 9 mM yields a ∼4% increase in blood plasma viscosity and a ∼3% increase in whole blood viscosity;[56] note for context that the relevant noninvasive physiological blood glucometry range is ∼1 to 50 mM.[57] In summary, glucose concentration is not the largest modifier of blood viscosity, although it does contribute. It seems possible that the effects of other relevant blood viscosity-modifying parameters can be accounted for, and thus glucose content may be derivable from measurements of blood viscosity.

To assess the potential of our methodology for blood glucometry measurements, we use the experimental parameters from our earlier publication (Ref. 9, rat blood) and from a more recent study (Ref. 28, mouse blood); both of these report correlation times of OCT backscattered radiation as a function of glucose concentration. We estimate the uncertainty of glucose concentration determination via $u(x) = \frac{\partial x}{\partial \tau_b} \cdot u(\tau_b)$, where x is the glucose concentration in units of molality, $u(\tau_b)$ is the uncertainty on the correlation times given in the papers, and the derivative can be estimated from the data in the papers. We then compare our estimates with the reported values of $u(x) = \pm 0.8$ mM[9] and $u(x) = \pm 5$ mM.[28]

Our uncertainty for the spectral width measurements no-flow conditions is 30 mHz (see Table 1); we assume the same for the case of measuring the power spectrum from blood under no-flow conditions.[†] In Ref. 9 (rat blood), the correlation time at $x = 20$ mM is 9.52 ms. We can calculate the expected uncertainty in correlation time measurement if our power spectrum technique was used: $u(\tau_b) = 2\pi(\tau_b)^2 u(HWHM_b) = 2\pi(9.52\ \text{ms})^2 \cdot 0.03\ \text{Hz} = 0.02$ ms. The corresponding expected uncertainty in glucose concentration measurement at $x = 20$ mM is thus $u(x) = \frac{\partial x}{\partial \tau_b} \cdot u(\tau_b) = 8.2\ \frac{\text{mM}}{\text{ms}} \cdot 0.02\ \text{ms} = 0.18$ mM, where we have used the table in Ref. 9 to estimate the derivative $\frac{\partial x}{\partial \tau_b}$. Comparing this with the initial reported precision of ±0.8 mM,[9] our estimated ∼4× improvement in $u(x)$ for rat blood is encouraging.

In Ref. 28 (mouse blood diluted with phosphate buffered saline), the correlation time at $x = 20$ mM is 7.1 ms (Fig. 5 of Ref. 28). Using this, we again calculate the expected uncertainty in correlation time measurement if our power spectrum measurement technique was used: $u(\tau_b) = 2\pi(\tau_b)^2 u(HWHM_b) = 2\pi(7.1\ \text{ms})^2 \cdot 0.03\ \text{Hz} = 0.01$ ms. The corresponding expected uncertainty in glucose concentration measurement at $x = 20$ mM is $u(x) = \frac{\partial x}{\partial \tau_b} \cdot u(\tau_b) = 2.0\ \frac{\text{mM}}{\text{ms}} \cdot 0.01\ \text{ms} = 0.02$ mM, where we have used the data in Fig. 5 of Ref. 28 to estimate the derivative $\frac{\partial x}{\partial \tau_b}$. This estimated ∼250× improvement in $u(x)$ for (diluted) mouse blood is also very encouraging.

Recapping, we have made OCT measurements of the power spectrum of backscattered radiation from aqueous glucose phantoms containing small microspheres in dilute concentration. This satisfies the conditions of our recently developed theory (dilute suspension noninteracting particles and single scattering regime).[12,35] We are currently refining our theory to describe more realistic tissue situations that include varying scatterer shape and concentration, inter-particle interaction, and multiple scattering effects; this is quite challenging and will be reported in separate forthcoming publications when successful.

5 Conclusions

The viscosity of turbid colloidal glucose solutions has been precisely and accurately determined from SD-OCT M-mode measurements and our recently developed OCT DLS model. Results for various glucose concentrations, flow speeds, and flow angles have been reported. The relative combined standard uncertainty $u_c(\eta)$ of our viscosity results was ∼1% for the no-flow case and ∼5% for the flow cases, representing a considerable improvement over the uncertainty reported in the literature. Available literature data for pure water and our measurements differ by <1% in the stagnant case and <1.5% in the flow cases, demonstrating good accuracy. The good agreement held across the entire glucose measurement concentration range by comparison with interpolated literature predictions. Based on the presented uncertainty analysis, our OCT power-spectrum-based approach, with its demonstrated good accuracy and low uncertainty, may contribute toward eventual noninvasive glucose measurements in medicine.

Disclosures

The authors have no competing interests to declare.

Acknowledgments

The authors thank Dr. Kostadinka Bizheva (University of Waterloo) for her help with the Fourier domain OCT system. This study was supported by the Canadian Institutes of Health Research (Grant No. 126172), the Ministry of Education and

[†]We realize the simplicity of this assumption, since blood is much more complex than microspheres in aqueous glucose solutions.

Science of the Russian Federation (Grant No. 14.B25.31.0015), and the Natural Sciences and Engineering Research Council of Canada/Canadian Institutes of Health Research through the Collaborative Health Research Program (CHRP Grant No. J365581-09).

References

1. W. J. Choi et al., "Cerebral capillary velocimetry based on temporal OCT speckle contrast," *Biomed. Opt. Express* **7**(12), 4859–4873 (2016).
2. Y. Wang et al., "In vivo total retinal blood flow measurement by Fourier domain Doppler optical coherence tomography," *J. Biomed. Opt.* **12**(4), 041215 (2007).
3. N. Weiss et al., "Measurement of biofilm growth and local hydrodynamics using optical coherence tomography," *Biomed. Opt. Express* **7**(9), 3508–3518 (2016).
4. T. E. de Carlo et al., "A review of optical coherence tomography angiography (OCTA)," *Int. J. Retina Vitreous* **1**(1), 5 (2015).
5. S. Huang et al., "In vivo imaging of retinal hemodynamics with OCT angiography and Doppler OCT," *Biomed. Opt. Express* **7**(2), 663–676 (2016).
6. L. Guo et al., "Optical coherence tomography angiography offers comprehensive evaluation of skin optical clearing in vivo by quantifying optical properties and blood flow imaging simultaneously," *J. Biomed. Opt.* **21**(8), 081202 (2016).
7. C. Apelian et al., "Dynamic full field OCT: metabolic contrast at subcellular level (conference presentation), *Proc. SPIE* **9697**, 969726 (2016).
8. C. E. Leroux et al., "Intracellular dynamics measurements with full field optical coherence tomography suggest hindering effect of actomyosin contractility on organelle transport," *Biomed. Opt. Express* **7**(11), 4501–4513 (2016).
9. H. Ullah et al., "Can temporal analysis of optical coherence tomography statistics report on dextrorotatory-glucose levels in blood?" *Laser Phys.* **21**(11), 1962–1971 (2011).
10. B. J. Berne and R. Pecora, *Dynamic Light Scattering: With Applications to Chemistry, Biology, and Physics*, Courier Corporation, New York (2000).
11. N. Weiss, T. G. van Leeuwen, and J. Kalkman, "Localized measurement of longitudinal and transverse flow velocities in colloidal suspensions using optical coherence tomography," *Phys. Rev. E* **88**(4), 042312 (2013).
12. I. Popov, A. S. Weatherbee, and I. A. Vitkin, "Dynamic light scattering arising from flowing Brownian particles: analytical model in optical coherence tomography conditions," *J. Biomed. Opt.* **19**(12), 127004 (2014).
13. N. Weiss, T. G. van Leeuwen, and J. Kalkman, "Simultaneous and localized measurement of diffusion and flow using optical coherence tomography," *Opt. Express* **23**(3), 3448–3459 (2015).
14. D. A. Boas, K. K. Bizheva, and A. M. Siegel, "Using dynamic low-coherence interferometry to image Brownian motion within highly scattering media," *Opt. Lett.* **23**(5), 319–321 (1998).
15. G. Popescu, A. Dogariu, and R. Rajagopalan, "Spatially resolved microrheology using localized coherence volumes," *Phys. Rev. E* **65**(4), 041504 (2002).
16. J. Lee et al., "Dynamic light scattering optical coherence tomography," *Opt. Express* **20**(20), 22262–22277 (2012).
17. R. K. Chhetri et al., "Imaging three-dimensional rotational diffusion of plasmon resonant gold nanorods using polarization-sensitive optical coherence tomography," *Phys. Rev. E* **83**(4), 040903 (2011).
18. G. Sloop, "A unifying theory of atherogenesis," *Med. Hypotheses* **47**(4), 321–325 (1996).
19. G. Sloop et al., "The role of chronic hyperviscosity in vascular disease," *Ther. Adv. Cardiovasc. Dis.* **9**(1), 19–25 (2015).
20. Y. Zhang et al., "Noninvasive blood glucose monitoring during oral intake of different sugars with optical coherence tomography in human subjects," *J. Biophotonics* **6**(9), 699–707 (2013).
21. Y. Liu et al., "In vitro assessment of effects of hyperglycemia on the optical properties of blood during coagulation using optical coherence tomography," *Lasers Med. Sci.* **30**(1), 413–420 (2015).
22. H. Ullah, F. Hussain, and M. Ikram, "Optical coherence tomography for glucose monitoring in blood," *Appl. Phys. B* **120**(2), 355–366 (2015).
23. M. Kinnunen et al., "In vitro studies toward noninvasive glucose monitoring with optical coherence tomography," *Appl. Opt.* **45**(10), 2251–2260 (2006).
24. R. O. Esenaliev et al., "Noninvasive monitoring of glucose concentration with optical coherence tomography," *Opt. Lett.* **26**, 992 (2001).
25. K. V. Larin et al., "Noninvasive blood glucose monitoring with optical coherence tomography: a pilot study in human subjects," *Diabetes Care* **25**, 2263–2267 (2002).
26. M. G. Ghosn, V. V. Tuchin, and K. V. Larin, "Depth-resolved monitoring of glucose diffusion in tissues by using optical coherence tomography," *Opt. Lett.* **31**, 2314–2316 (2006).
27. H. Ullah et al., "Quantification of glucose levels in flowing blood using M-mode swept source optical coherence tomography," *Laser Phys.* **22**, 797–804 (2012).
28. L. R. De Pretto et al., "Optical coherence tomography for blood glucose monitoring in vitro through spatial and temporal approaches," *J. Biomed. Opt.* **21**, 086007 (2016).
29. J. Solanki et al., "Blood glucose monitoring in human subjects using optical coherence tomography," *J. Opt.* **41**, 127–133 (2012).
30. BIPM, IEC, ILAC, IFCC, IUPAC, ISO, OIML, and IUPAP, "Evaluation of measurement data—guide to the expression of uncertainty in measurement GUM 1995 with minor corrections," Joint Committee for Guides in Metrology, JCGM 100, 2008, http://www.BIPM.org/utils/common/documents/jcgm/JCGM_101_2008_E.pdf (23 February 2017).
31. A. V. Bui and M. H. Nguyen, "Prediction of viscosity of glucose and calcium chloride solutions," *J. Food Eng.* **62**(4), 345–349 (2004).
32. V. R. N. Telis et al., "Viscosity of aqueous carbohydrate solutions at different temperatures and concentrations," *Int. J. Food Prop.* **10**(1), 185–195 (2007).
33. R. Moreira, F. Chenlo, and G. Pereira, "Viscosities of ternary aqueous solutions with glucose and sodium chloride employed in osmotic dehydration operation," *J. Food Eng.* **57**(2), 173–177 (2003).
34. W. M. Haynes, Ed., "Concentrative properties of aqueous solutions: density, refractive index, freezing point depression, and viscosity," in *CRC Handbook of Chemistry and Physics*, 92nd ed., CRC Press/Taylor and Francis, Boca Raton, Florida, Internet Version (2016).
35. I. Popov and A. Vitkin, "Dynamic light scattering by flowing Brownian particles measured with optical coherence tomography: impact of the optical system," *J. Biomed. Opt.* **21**(1), 017002 (2016).
36. J. Tokayer et al., "Blood flow velocity quantification using split-spectrum amplitude-decorrelation angiography with optical coherence tomography," *Biomed. Opt. Express* **4**(10), 1909–1924 (2013).
37. N. Uribe-Patarroyo, M. Villiger, and B. E. Bouma, "Quantitative technique for robust and noise-tolerant speed measurements based on speckle decorrelation in optical coherence tomography," *Opt. Express* **22**(20), 24411–24429 (2014).
38. B. Davoudi et al., "Noninvasive in vivo structural and vascular imaging of human oral tissues with spectral domain optical coherence tomography," *Biomed. Opt. Express* **3**(5), 826–839 (2012).
39. From the acceptance test report (data sheet) for the light source SU1024LDH-1.7, UTC Aerospace Systems.
40. J. E. Bertie and Z. Lan, "Infrared intensities of liquids XX: the intensity of the OH stretching band of liquid water revisited, and the best current values of the optical constants of $H_2O(l)$ at 25°C between 15,000 and 1 cm^{-1}," *Appl. Spectrosc.* **50**(8), 1047–1057 (1996).
41. A. H. Harvey, J. S. Gallagher, and J. L. Sengers, "Revised formulation for the refractive index of water and steam as a function of wavelength, temperature and density," *J. Phys. Chem. Ref. Data* **27**(4), 761–774 (1998).
42. Bangs laboratories data sheet for 215.1 nm diameter polystyrene microspheres.
43. J. M. Schmitt, A. Knüttel, and M. Yadlowsky, "Confocal microscopy in turbid media," *JOSA A* **11**(8), 2226–2235 (1994).
44. Y. Aizu, T. Ushizaka, and T. Asakura, "Measurements of flow velocity in a microscopic region using a transmission grating: a differential type," *Appl. Opt.* **24**(5), 627–635 (1985).
45. S. M. Abrarov and B. M. Quine, "Efficient algorithmic implementation of the Voigt/complex error function based on exponential series approximation," *Appl. Math. Comput.* **218**(5), 1894–1902 (2011).
46. M. R. Zaghloul and A. N. Ali, "Algorithm 916: computing the Faddeyeva and Voigt functions," *ACM Trans. Math. Softw.* **38**(2), 15 (2011).

47. S. M. Abrarov, "The Voigt/complex error function (second version)," 2016, https://www.mathworks.com/matlabcentral/fileexchange/47801-the-voigt-complex-error-function--second-version- (2 June 2017).
48. S. G. Johnson, "Faddeeva package," 2012, http://ab-initio.mit.edu/wiki/index.php/Faddeeva_Package (2 June 2017).
49. D. A. Berstad et al., "Accurate measurements of the viscosity of water in the temperature range 19.5–25.5°C," *Phys. A* **151**(2–3), 246–280 (1988).
50. J. F. Comesaña et al., "Densities and viscosities of ternary systems of water + glucose + sodium chloride at several temperatures," *J. Chem. Eng. Data* **48**(2), 362–366 (2003).
51. Data sheet for BP209-IR scanning slit optical beam profiler, Thorlabs Inc.
52. Data sheet for syringe pump NE-4002X, New Era Pump Systems Inc.
53. A. Weatherbee et al., "Probability density function formalism for optical coherence tomography signal analysis: a controlled phantom study," *Opt. Lett.* **41**(12), 2727–2730 (2016).
54. T. I. Török, J. A. Rard, and D. G. Miller, "Viscosities, electrolytic conductivities, and volumetric properties of HCl-MCl_X-H_2O as a function of temperature up to high molal ionic strengths," *Fluid Phase Equilib.* **88**, 263–275 (1993).
55. G. Cokelet, "Hemorheology and hemodynamics," in *Colloquium Series on Integrated Systems Physiology: From Molecule to Function*, Vol. **3**, pp. 1–140, Morgan & Claypool Life Sciences, Williston, Vermont (2011).
56. K. Koltai et al., "The effect of blood glucose levels on hemorheological parameters, platelet activation and aggregation in oral glucose tolerance tests," *Clin. Hemorheol. Microcirc.* **35**(4), 517–525 (2006).
57. A. E. Kitabchi et al., "Hyperglycemic crises in adult patients with diabetes," *Diabetes Care* **32**(7), 1335–1343 (2009).

Andrew Weatherbee is a MSc candidate in the Department of Medical Biophysics, the University of Toronto. He completed his honors BSc degree in physics from Western University. His research experience covers data analysis and processing using MATLAB® and LabVIEW, meteor tracking and detection using infrasonic microphones and radar antennas, and microfabrication of small particles using photolithography. His current research focuses on practical applications of dynamic light scattering techniques under optical coherence tomography conditions.

Ivan Popov received his master's degree in radio physics and his PhD in optics from St. Petersburg State University, Russia, in 1972 and 1979, respectively, and his DSc degree in optics from the Institute of Fine Mechanics and Optics, St. Petersburg, Russia, in 2000. His area of expertise includes optics of speckles, noncontact techniques of motion measurement, and biomedical applications of optical coherence domain techniques. He is currently with the Biophotonics Group, University Health Network, Toronto, Canada.

Alex Vitkin is a professor of medical biophysics and radiation oncology at the University of Toronto, a senior scientist at University Health Network, and a board-certified clinical medical physicist at Princess Margaret Cancer Centre (all in Toronto, Canada). He has published more than 170 papers and book chapters on biophotonics. He is also a topical editor of *Optics Letters*, a fellow of OSA and SPIE, and a visiting professor at the Nizhny Novgorod State Medical Academy, Russia.